



## Airfoil-shaped self-agitator for convective heat transfer enhancement

Zheng Li<sup>a</sup>, Xianchen Xu<sup>a</sup>, Kuojiang Li<sup>a</sup>, Yangyang Chen<sup>a</sup>, Guoliang Huang<sup>a,\*\*</sup>,  
Chung-Lung Chen<sup>a,\*</sup>, Chien-Hua Chen<sup>b</sup>

<sup>a</sup> Mechanical and Aerospace Engineering, University of Missouri-Columbia, Columbia, MO, 65201, USA

<sup>b</sup> Advanced Cooling Technologies, Inc. Lancaster, Pennsylvania, 17601, USA

### ABSTRACT

A novel airfoil-shaped self-agitator is developed for airside heat transfer enhancement within rectangular heatsink channels. Due to fluid-structure interaction, the airfoil-shaped self-agitator oscillates and generates vortices that improve mixing within the channel and thus improve the heat transfer. The fluid-structure interaction is simulated with the fully coupled method of remeshing. Numerical results show that the self-agitator can generate out-of-phase heaving and rotating motions to enhance heat transfer by 27% without additional power costs and the Nusselt number can be improved by 53% at the same Reynolds number. To investigate the fundamental aspects of the convective heat transfer enhancement with vortex generation, modal analysis is performed for the vorticity and temperature fields with dynamic modal decomposition. Instantaneous results can be constructed with steady mode and six dominant unsteady modes, while the steady mode results can be used to predict the average thermal performance. A prototype of the self-agitator is fabricated and tested experimentally for concept demonstration and validation. The experimental results show the self-agitator can improve the air-side thermal performance in the rectangular channel significantly without additional pumping power.

### 1. Introduction

Air-side convective heat transfer plays an important role in many industries such as power generation, HVAC, and electronic component cooling. The two types of convective heat transfer are natural convection and forced convection, which are distinguished by the external pumping power [1–4]. In this article, only forced convection is considered.

Many strategies exist to enhance air-side heat transfer, such as offset strip fins, T-mixers, and Dean flow in curved pipes. Because these strategies enhance heat transfer by modifying the flow channel to generate vortices, implementation may involve the replacement of the entire design of a heat exchanger. This additional cost could limit their practicality. On the other hand, straight plate fins, without flow path modification are widely used as air-side heat exchangers. The alternative strategy for enhancing heat transfer would be adding devices of vortex generation to the current existing heat exchanger rather than replacing it.

Active vortex generators have been employed to enhance heat transfer in different applications [5–8]. These active vortex generators can be retrofitted to existing heat exchangers, and their oscillating frequencies directly affect the thermal performance. However, active vortex generators require an additional power supply system to drive the structural oscillation.

In recent years, fluid-structure interaction (FSI) has been of practical interest in many engineering fields [9–15]. FSI is the coupling between fluid dynamics and structural dynamics, usually leading to undesirable consequences including divergence, control reversal, and flutter. In aeroelasticity, flutter is a self-excited and potentially destructive oscillatory instability, in which aerodynamic forces on a flexible body couple with its natural modes of vibration to produce oscillatory motions with increasing amplitude. Because of this feature, wings, airfoils, and bridges under aerodynamic loadings must be carefully designed to avoid flutter. However, it has also been shown that those self-excited oscillatory motions are beneficial in energy harvesting [16,17], and heat transfer enhancement [18–22]. Current research on FSI for heat transfer enhancement predominantly employs elastic structures and the Young's modulus effect to the thermal performance has been discussed [23]. One unique FSI concept using an elastic beam with a rotatable rigid structure has been developed for acoustic applications [24,25]. In this article, we apply this unique design to develop a novel self-agitator for heat transfer enhancement for the first time. Numerical and experimental investigations are carried out and the results show that self-agitator can improve performance of air-side heat exchangers.

Vortices can improve the internal convective heat transfer because they can interrupt the thermal boundary layer [26,27]. However, the fundamental relation between vortices and thermal performance has not been addressed. In recent years, modal analysis has been introduced

\* Corresponding author.

\*\* Corresponding author.

E-mail addresses: [HuangG@Missouri.edu](mailto:HuangG@Missouri.edu) (G. Huang), [ChenCL@Missouri.edu](mailto:ChenCL@Missouri.edu) (C.-L. Chen).

Nomenclature			
$c_p$	specific heat (J/K)	$T$	temperature (K)
$h$	local heat transfer coefficient (W/mK)	$u$	velocity in x direction (m/s)
$H$	2-D channel height (m)	$u_0$	rotation center displacement (m)
$h_s$	agitator displacement (m)	$\vec{u}_s$	motion of agitator (m)
$k$	thermal conductivity (W/m <sup>2</sup> K)	$v$	velocity in y direction (m/s)
$k_h$	linear translational spring constant (N/m <sup>2</sup> )	$\beta_h$	nonlinear translational spring constant (N/m <sup>4</sup> )
$k_\theta$	torsional spring constant (N)	$\lambda$	Lame's first parameter (Pa)
$L$	2-D channel length (m)	$\mu_s$	Lame's second parameter (Pa)
$Nu$	Nusselt number (-)	$\mu$	viscosity (Pa*s)
$Re$	Reynolds number (-)	$\rho_0$	air density (kg/m <sup>3</sup> )
$p$	pressure (Pa)	$\rho_s$	solid density (kg/m <sup>3</sup> )
		$\theta$	rotation angle (-)

to understand the coherent structures in the fluid flow, as discussed in a comprehensive review paper [28]. In this article, dynamic modal decomposition [29–31] is performed with the transient numerical results in vorticity and temperature fields to explore the fundamental understanding of the convective heat transfer.

### 2. Simplified model

An air-side straight plate fin heat exchanger used for baseline performance is shown in Fig. 1(a). The bottom boundary is a constant temperature heat source, and the top boundary is an insulation plate. Heat rejection is dependent on the air flow in the channel with convective heat transfer.

As shown in Fig. 1(b), novel self-agitators are placed in the straight plate fin heat exchanger to improve the thermal performance. These agitators have three components: a support, a beam, and an airfoil-shaped agitator. They oscillate in the channel due to fluid-structure interaction.

The support and beam are simplified as a mass-spring system [24,25], which is shown in Fig. 2. A two-dimensional laminar air flow for an agitator between two parallel plates is simulated in this study. The governing equations for the fluid flow and heat transfer can be written as

$$\frac{\partial u}{\partial x} + \frac{\partial v}{\partial y} = 0, \tag{1}$$

$$\rho_0 \left( \frac{\partial u}{\partial t} + u \frac{\partial u}{\partial x} + v \frac{\partial u}{\partial y} \right) = -\frac{\partial p}{\partial x} + \mu \left( \frac{\partial^2 u}{\partial x^2} + \frac{\partial^2 u}{\partial y^2} \right), \tag{2}$$

$$\rho_0 \left( \frac{\partial v}{\partial t} + u \frac{\partial v}{\partial x} + v \frac{\partial v}{\partial y} \right) = -\frac{\partial p}{\partial y} + \mu \left( \frac{\partial^2 v}{\partial x^2} + \frac{\partial^2 v}{\partial y^2} \right), \tag{3}$$

$$\rho_0 c_p \left( \frac{\partial T}{\partial t} + u \frac{\partial T}{\partial x} + v \frac{\partial T}{\partial y} \right) = k \left( \frac{\partial^2 T}{\partial x^2} + \frac{\partial^2 T}{\partial y^2} \right), \tag{4}$$

$$\begin{cases} x = 0, & u = u_{in}, & v = 0, & T = T_{in} \\ x = L, & p = p_{ambient}, & \partial T / \partial x = 0 \\ y = 0, & u = 0, & v = 0, & T = T_{wall} \\ y = H, & u = 0, & v = 0, & T = T_{wall} \end{cases} \tag{5}$$

where  $u$  and  $v$  are velocities in the  $x$ - and  $y$ -directions, respectively.  $T$  and  $p$  are the fluid temperature and pressure.  $k$ ,  $\rho_0$ ,  $c_p$  and  $\mu$  are thermal conductivity, density, specific heat, and viscosity determined by the fluid properties, respectively.

The equations of motion for the agitator can be written as,

$$(\lambda + \mu_s) \nabla \nabla \cdot \vec{u}_s + \mu_s \nabla^2 \vec{u}_s = \rho_s \ddot{\vec{u}}_s, \tag{6}$$

where motion displacement  $\vec{u}_s = [u_1, u_2]^T$ . The velocity and stress fields on the fluid-solid boundaries must be continuous as

$$\begin{cases} \vec{v} = \dot{\vec{u}}_s \\ \vec{\sigma} \cdot \vec{n} = \vec{T} \cdot \vec{n} \end{cases}, \tag{7}$$

where the stress in the solid is  $\vec{\sigma} = \mu_s [(\nabla \vec{u}_s)^T + \nabla \vec{u}_s] + \frac{\lambda}{2} \text{tr} [(\nabla \vec{u}_s)^T + \nabla \vec{u}_s] \vec{I}$  and the stress in the fluid is  $\vec{T} = -p \vec{I} + \mu [(\nabla \vec{v})^T + \nabla \vec{v}] - \frac{2}{3} \mu (\nabla \cdot \vec{v}) \vec{I}$  with  $\vec{v} = [u, v]^T$ . Eq. (7) describes the fluid-structural coupling effects in the numerical simulations.

The force and torque induced by the deformations of the mass-spring system to the self-agitator are directly related to the displacement of the rotation center,  $u_0$ , and rotation angle,  $\theta$  of the airfoil as

$$F = k_h u_0 + \beta_h u_0^3, \tag{8}$$

$$M = k_\theta \theta, \tag{9}$$

where  $k_h$ ,  $\beta_h$  and  $k_\theta$  are the linear spring constant, nonlinear spring constant, and spring constant for torque determined by material and size. The force and torque are applied along a voided circle at the rotation center of the airfoil through a rigid connector boundary condition. It should be mentioned that a nonlinear spring constant  $\beta_h$  is introduced in Eq. (8) to achieve limit cycle oscillations, and to prevent the

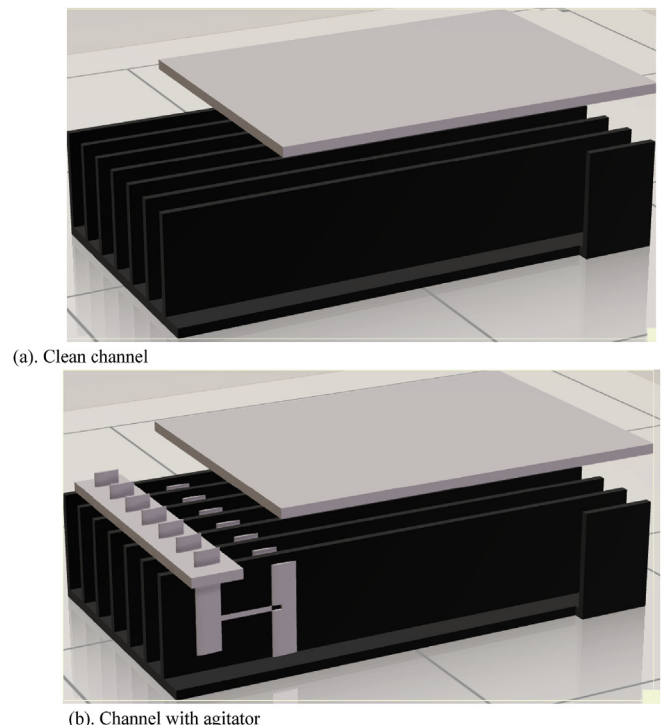


Fig. 1. Channels without and with self-agitator.

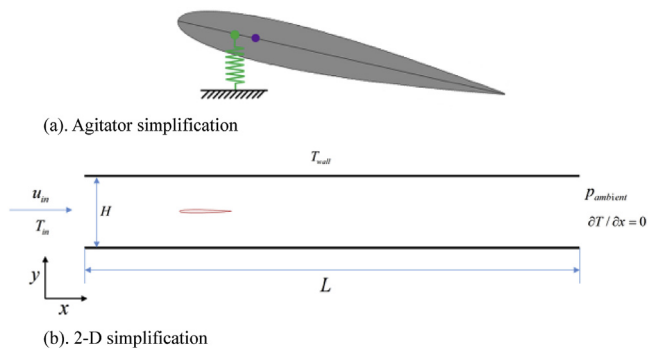


Fig. 2. Physical model.

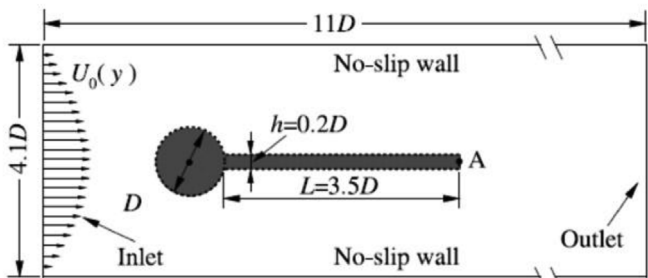


Fig. 3. Flow-induced vibration of an elastic beam behind a cylinder.

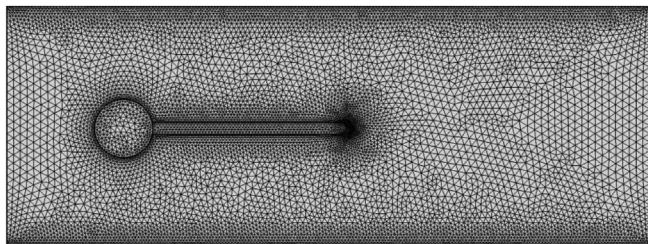


Fig. 4. Grid setting for an elastic beam behind a cylinder.

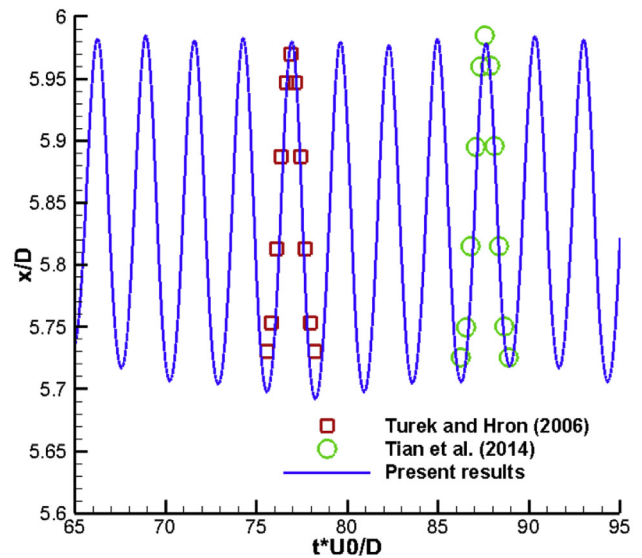
contact of the airfoil and channel wall boundaries.

### 3. Validations of numerical method and experimental setups

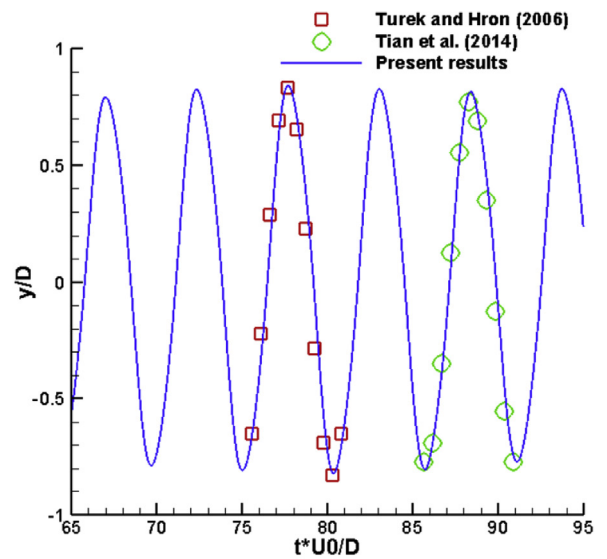
In this article, both experimental and numerical investigations are performed to study the self-agitator for convective heat transfer enhancement. The numerical method for the FSI simulation and experimental setups for the convective heat transfer testing are validated in this section.

#### 3.1. Numerical method for fluid structure interaction

To simulate the FSI process with large deformation, numerical tools exist including remeshing and the immersed boundary method [32], [33]. In the remeshing method, the fluid region and solid region are given independent meshes. Remeshing occurs when the mesh quality is lower than the chosen criteria. For the immersed boundary method, the whole region is first treated as a fluid, with a fluid mesh, and the solid region has an additional mesh overlapping the fluid mesh. In this article, the remeshing method in the commercial software COMSOL Multiphysics is employed to simulate the FSI process with large deformation. To verify the numerical method, flow-induced vibration of an elastic beam behind a cylinder (shown in Fig. 3) is calculated and the results are compared with available references [34], [35]. An elastic beam is attached to a stationary rigid cylinder, and the geometric



(a) Horizontal displacement



(b) Vertical displacement

Fig. 5. Structure displacements compared with reference results.

Table 1

Results comparison in flow-induced vibration of the beam attached to a cylinder.

		$A_m/D$	St	$C_D$
$Re = 100 \rho_s/\rho_f = 10$	Turek and Hron (2006)	0.83	0.190	4.13
	Tian et al. (2014)	0.78	0.190	4.11
	Present results	0.81	0.183	4.05
$Re = 200 \rho_s/\rho_f = 1$	Turek and Hron (2006)	0.32	0.29	2.16
	Tian et al. (2014)	0.36	0.26	2.30
	Present results	0.32	0.25	2.20

parameters are shown in Fig. 3. The top and bottom boundaries are defined with a non-slip condition, while the inlet has a parabolic velocity profile. The average inlet velocity is  $\bar{U}_0$ , which is used to calculate the Reynolds number ( $Re$ ). Two cases are in consideration for validation: (1)  $Re = 100$  while the ratio between structure and fluid densities is  $\rho_s/\rho_f = 10$ ; (2)  $Re = 200$  and  $\rho_s/\rho_f = 1$ . The non-dimensionalized

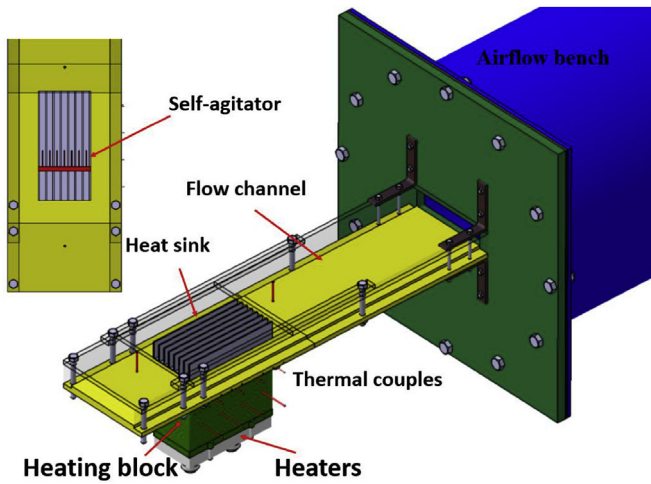


Fig. 6. Model for the experimental setup.

Young's Modulus is defined as  $E^* = E/\rho_f \bar{U}_0^2 = 1400$ . After conducting a grid independent study, the grid shown in Fig. 4 is selected.

Fig. 5 shows the horizontal and vertical displacements for the  $Re = 100$  condition for the chosen point A (marked in Fig. 3) which agree very well with previous works [34], [35]. The amplitude of the free end in y-direction denoted by  $A_m$ , the Strouhal number defined as  $St = fD/\bar{U}_0$  ( $f$  is the oscillation frequency), and the average drag coefficient  $C_D = \bar{F}_x/(0.5\rho_f \bar{U}_0^2 D)$  are compared with reference results as shown in Table 1 for the two conditions. Very good agreements are obtained for all these three parameters and therefore, the numerical method is valid for solving the FSI with large deformations.

### 3.2. Airflow bench test for convective heat transfer

Fig. 6 shows a model of the experimental setup of the airflow bench test for convective heat transfer measurement. An airflow bench with a standard flow ranging from 3 to 150 CFM (150 CFM Chamber, Airflow Measurement Systems) is used to provide quantitative cooling air into the flow channel, which is composed of a 3D printed base material and side walls with a transparent top. Heat sink performance enhancement with self-agitators is quantified in terms of increased rejected heat over a range of flow rates compared to the baseline flow in the absence of the self-agitators. Heat from the heating block is removed through the heat sink with convective heat transfer. The heat sink to be tested is made of aluminum alloy with thermal conductivity of 167 W/mK. It has seven channels with a gap spacing of 6.6 mm, 21.8 mm height and 121.9 mm length, while the fin thickness is 1.5 mm. The heating block is made of aluminum with a thermal conductivity of 120 W/mK while two resistive heaters are powered by a power supply providing heat flux through the aluminum block to the bottom of the heat sinks. Fiberglass is used for insulation and thermocouples are used to measure the

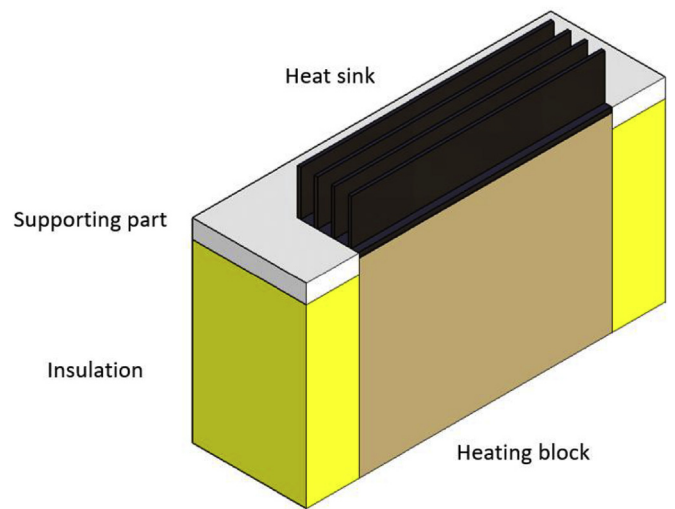


Fig. 8. Simplified model for numerical study to verify the experimental setup.

temperature distribution at each height. This was averaged into one representative temperature for each height. Fourier's law of heat conduction is used to find the heat flow through the substrate, and thus the heat supplied to the heat sink. It is necessary to point out that heat loss still exists even though insulation is used in the system.

Fig. 7 shows the experimental lab setup and it has been used to test different air-side convective heat transfer conditions [36–38]. Experimental and numerical results are compare for the clean channel condition to validate this experimental setup. Fig. 8 shows the simplified model for numerical simulation and only half of the test section is considered because of the symmetry condition. Fiberglass insulation covers most of the side area of the heating block to lower the heat loss. The rest of heating block sides are attached to the flow channel made of 3D printed material. The heating block keeps the heat sink base average temperature 30 °C higher than the inlet temperature in both numerical and experimental investigations.

Rejected heat, which is defined as the average heat flux of the heat sink, is the critical parameter for the performance to reflect the amount of heat that can be rejected from heat sink. Fig. 9(a) shows the numerical and experimental rejected heat comparison for different velocities where good agreements are achieved. Rejected heat from heat sink is lower than that from the heating block bottom because of the heat loss from the sides. The fin surface temperature is not constant and is lower than the heat sinks base temperature with regards to the fin efficiency. Table 2 shows the fin efficiency and heat loss for different inlet velocity conditions. The heat loss for different velocities are all around 300 W/m<sup>2</sup>. With an improved convective heat transfer, the heat transfer coefficient will be higher. Consequently, the fin efficiency will be lower, which will decrease the rejected heat improvement. Therefore, we need to eliminate the fin efficiency and heat loss effects to

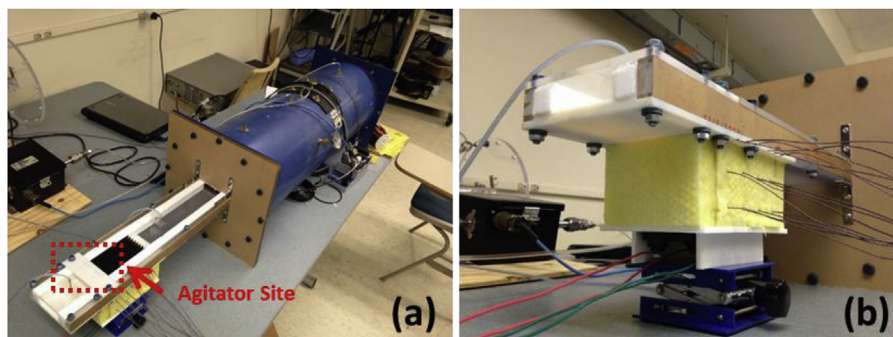
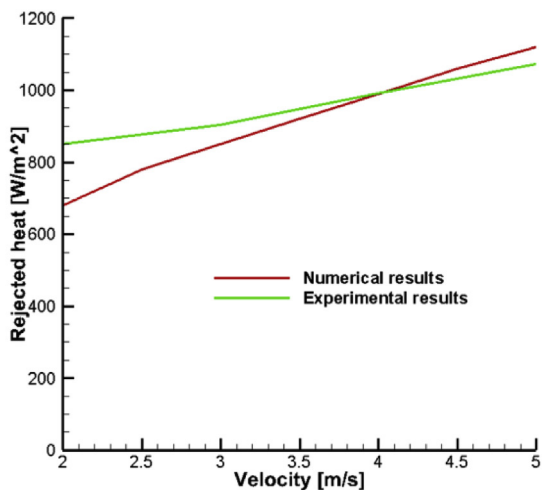
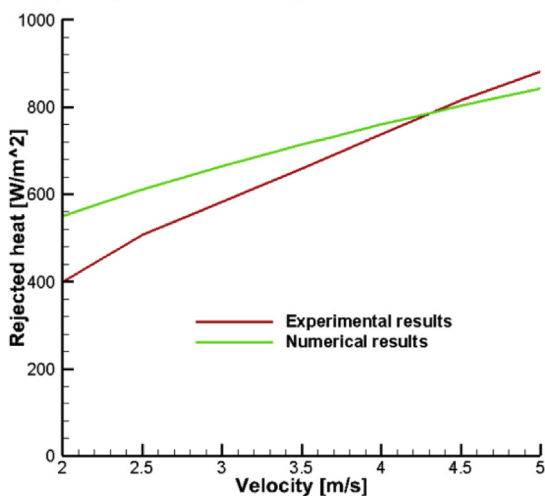


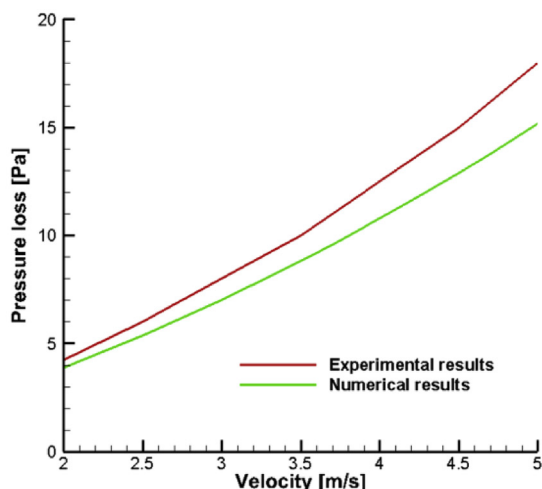
Fig. 7. In lab airflow bench setup for convective heat transfer test.



(a) Reject heat comparison with heat loss



(b) Rejected heat with constant wall temperature



(c) Pressure loss

Fig. 9. Numerical and experimental results comparison for clean channel.

make a fair evaluation of the thermal performance.

To achieve the constant fin temperature results based on the current experimental results, we need to calculate the heat transfer coefficient (HTC) in the experiment first without considering heat loss and fin

Table 2

Fin efficiency and heat loss for clean channel.

Velocity (m/s)	2	3	4	5
Heat loss (W/m <sup>2</sup> )	308.9	305.1	307.0	310.5
Fin efficiency (%)	98.2	97.6	97.4	97.3

Table 3

Relative uncertainty of rejected heat.

Inlet velocity (m/s)	2.02	2.65	3.15	3.81	4.39	4.81	5.51	5.79
Rejected heat uncertainty (%)	5.04	4.48	4.25	3.74	3.37	3.17	2.91	2.79

Table 4

Relative uncertainty of overall Nusselt number.

Re	1310	1717	2043	2463	2742	3114	3568	3745
Nu uncertainty (%)	6.05	5.25	4.90	4.30	3.87	3.63	3.31	3.18

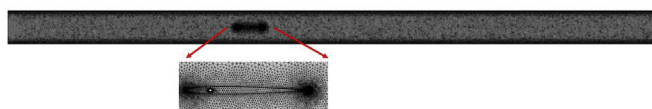


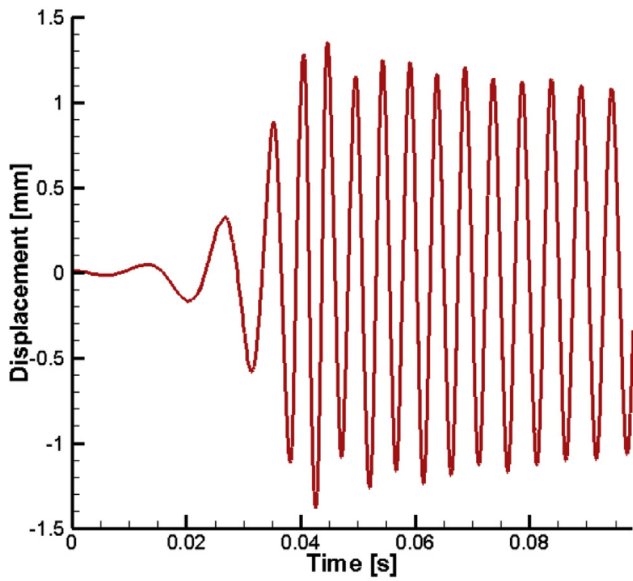
Fig. 10. Grid setting for self-agitator.

efficiency. It is calculated by the following steps: (1) Calculate the rejected heat in the heating block (Heat 1); (2) Use the rejected heat and inlet velocity to obtain the outlet temperature; (3) Estimate the Logarithmic mean temperature difference (LMTD) by assuming the wall temperature is the heating block average base temperature; (4) Divide the rejected heat by LMTD to obtain HTC. After this, we can use the calculated HTC to estimate fin efficiency (Wang & Chi, 2000). It is necessary to point out that the HTC in this step differs from the realistic one, because the rejected heat in the calculation process includes the heat loss component which would cause error in the fin efficiency calculation. However, this error is acceptable because it is less than 3% for all experimental results. Referring to the numerical results, the realistic rejected heat from heat sink (Heat 2) can be calculated by Heat 1 minus 300 W/m<sup>2</sup>. Lastly, Heat 2 is divided by fin efficiency to estimate the rejected heat with constant wall temperature (Heat 3). On the other hand, the constant fin temperature condition is solved numerically for different conditions. Fig. 9(b) shows the numerical and experimental rejected heat comparison for the constant fin temperature condition, where good agreements are achieved. Besides the rejected heat, the total pressure loss between the inlet and outlet of the heat sink is another critical parameter to evaluate the thermal performance. Fig. 9(c) indicates that the numerical and experimental results are quite close to each other for different velocities. Therefore, the experimental setup for convective heat transfer testing is reliable regarding the rejected heat and total pressure loss comparisons between numerical and experimental results.

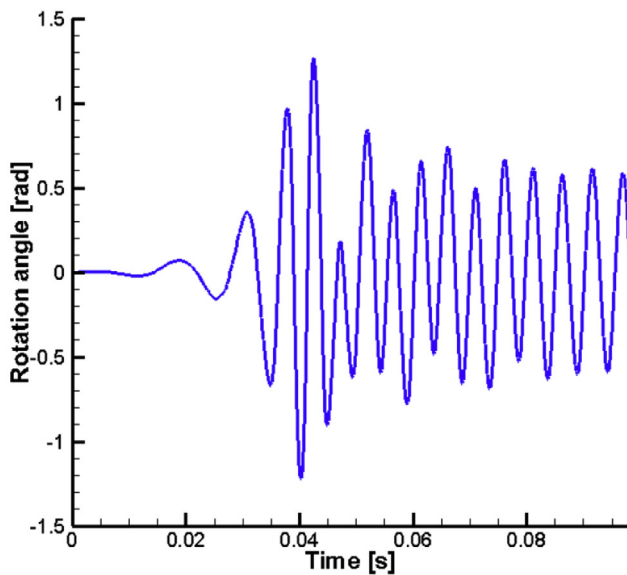
The uncertainty for the present experiment setup is estimated using the standard approach proposed by Moffat et al. [39]. The uncertainty estimations range from 2.79% to 5.04% for the rejected heat and 3.18%–6.05% for the overall Nusselt number. The highest uncertainties were associated with the lowest flow velocity and Reynolds number. These results are tabulated in Table 3 and Table 4.

#### 4. Numerical results and discussions

In the simplified 2D model, the channel height,  $H$ , and channel length,  $L$ , are 5 mm and 100 mm, respectively. The agitator is 4 mm in length with a NACA0012 airfoil shape, and the spring connection to the agitator is 0.8 mm to the leading edge. The wall temperature is



(a). Rotation center heave motion



(b). Rotation motion

Fig. 11. Self-agitator motion in test case 1.

308.15 K and the inlet temperature is 298.15 K. Two test cases with inlet velocities of 3.136 m/s and 3.763 m/s are solved. The corresponding Reynolds numbers of 2000 and 2400, respectively, are treated in the laminar region.

4.1. Test case 1 results

The self-agitator motions have two parts: heave and rotation around the connector to the spring system. In test case 1 the inlet velocity is 3.136 m/s, while  $k_r k_h$ ,  $\beta_h$  and  $k_o$  are 67.1 N/m<sup>2</sup>,  $3.69 \times 10^8$  N/m<sup>4</sup> and  $5 \times 10^{-5}$  N, respectively. The self-agitator oscillates in the channel without touching the boundary. This case is solved with the remeshing method, which is validated in section 3.1. After the grid independent study, the total number of elements is  $98.640 \times 10^3$ , which is shown in Fig. 10. Structured meshes are employed for the boundary layer while the rest of the region uses unstructured meshes. During the remeshing process, the total number of elements only changes slightly. This remeshing method with similar grid settings has been employed to solve

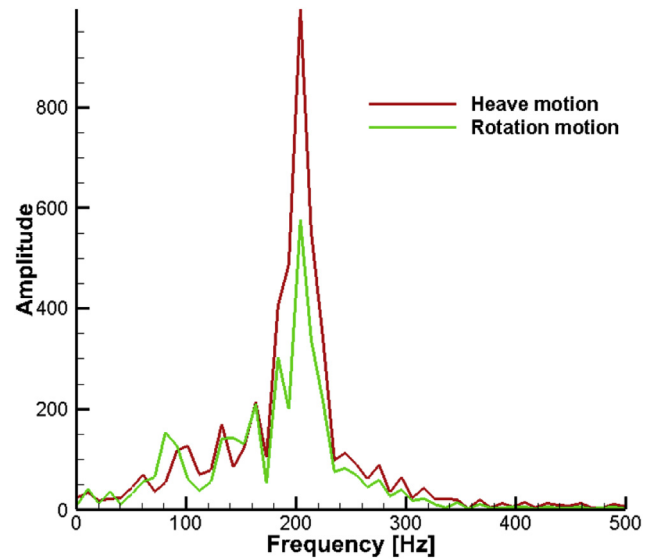


Fig. 12. Fourier analysis results in test case 1.

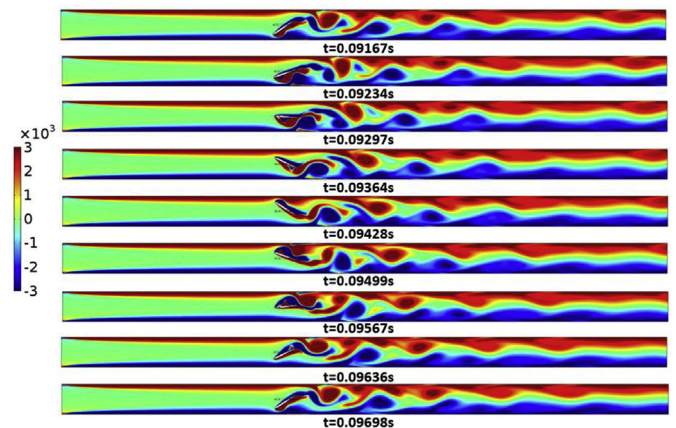


Fig. 13. Vorticity field in test case 1.

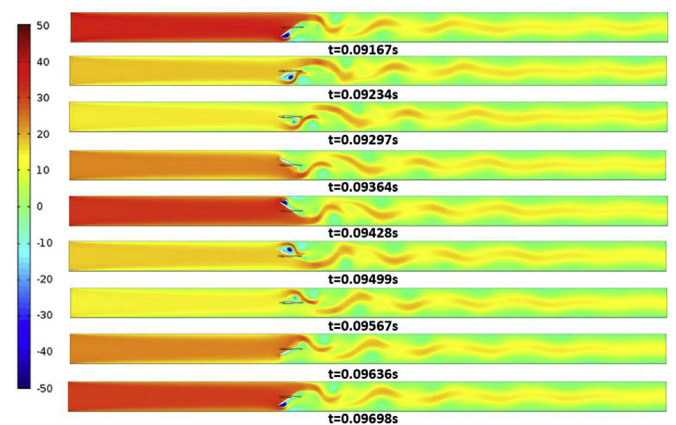


Fig. 14. Gauge pressure field in test case 1.

the FSI process with elastic self-agitator, and more details about grid independent study can be found in our pervious article [23].

Fig. 11 shows the heave and rotation motions for test case 1. Clockwise rotation around the rotation center results in a negative angle. With increasing time, the rotation center heave motion ranges from  $-1.1$  mm to  $1.1$  mm, while rotation motion is from  $-0.6$  rad to  $0.6$  rad. These two motions are out-of-phase because the maximum

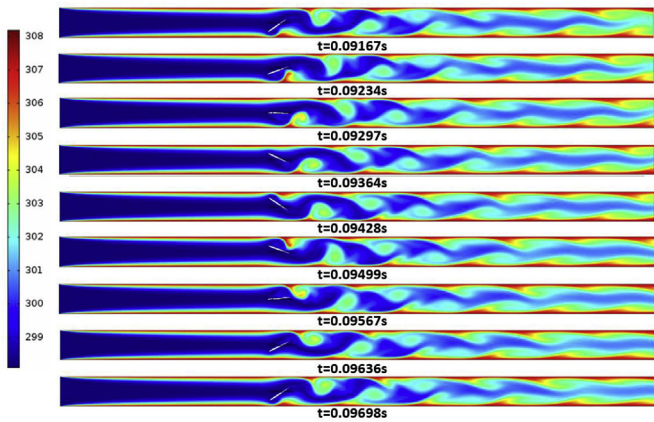
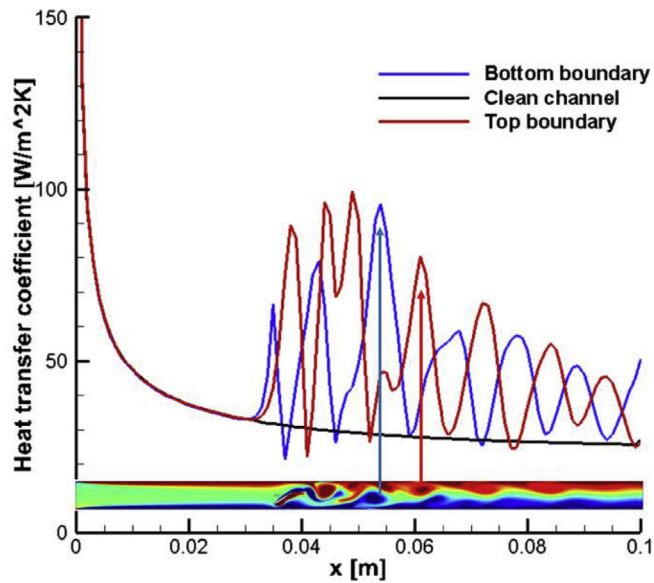
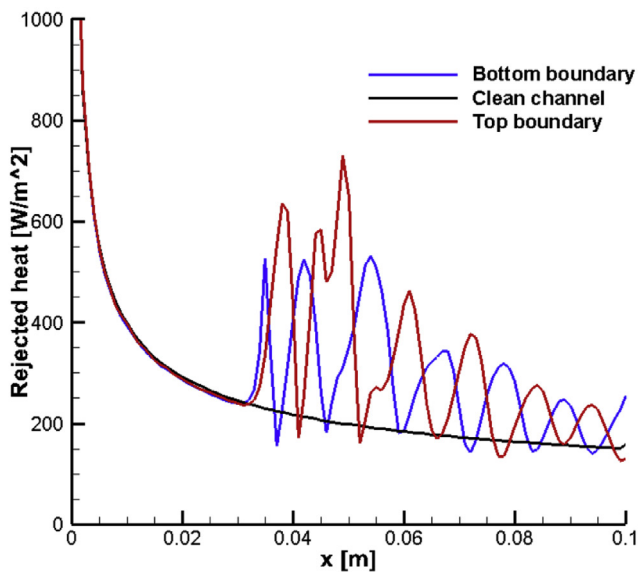


Fig. 15. Temperature field in test case 1.

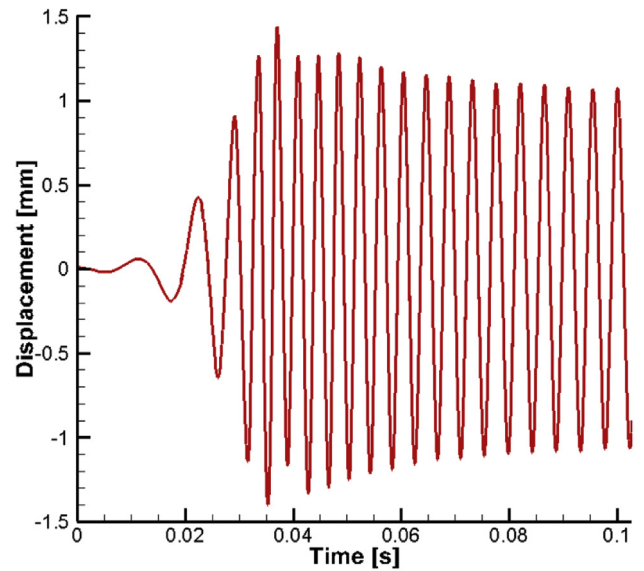


(a). Heat transfer coefficient comparison

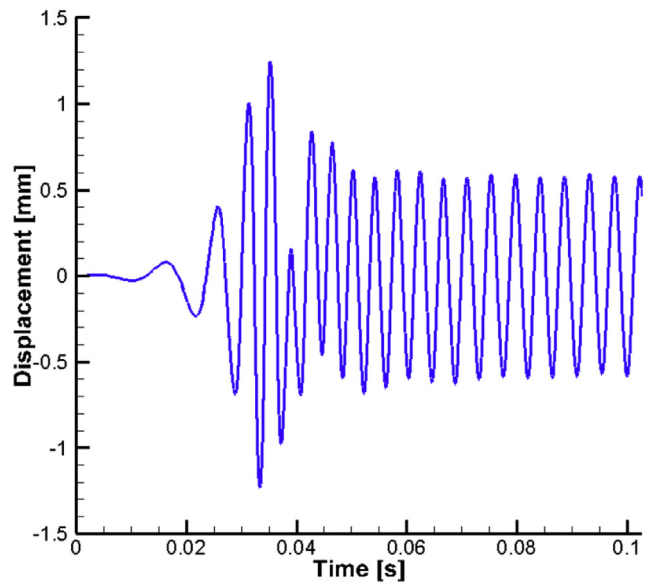


(b). Rejected heat comparison

Fig. 16. Local thermal performance comparison in test case 1.



(a). Rotation center heave motion



(b). Rotation motion

Fig. 17. Self-agitator motion in test case 2.

heave motion and minimum rotation angle take place at the same time. Fourier analysis in Fig. 12 shows the results are periodic at 200 Hz.

To investigate the principle of self-agitation for heat transfer enhancement, the vorticity field, pressure field, and temperature field for one period are included in Figs. 13–15. Because heave and rotation motions are out-of-phase, the leading edge is closest to the boundary when the heave motion reaches extreme values. For the vorticity field shown in Fig. 13, one counterclockwise vortex begins to form at the leading edge and another clockwise vortex forms at the channel bottom, when the leading edge is closest to the channel bottom. Then the vortices grow larger with time until the self-agitator reaches the middle of the channel; after that, the generated vortices begin to shed to the downstream direction. When the leading edge is closest to the top boundary, new vortices begin to form at the leading edge and at the boundary. Then, the vortices grow and shed to the downstream direction when the self-agitator reaches the bottom.

Fig. 14 shows the gauge pressure fields in one period for test case 1. When the leading edge is closest to the channel bottom, a negative gauge pressure region appears during the vortex generating process.

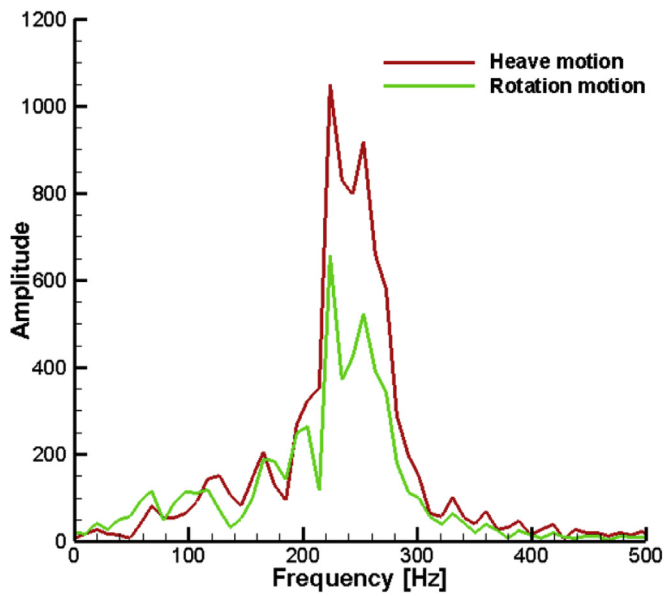


Fig. 18. Fourier analysis results in test case 2.

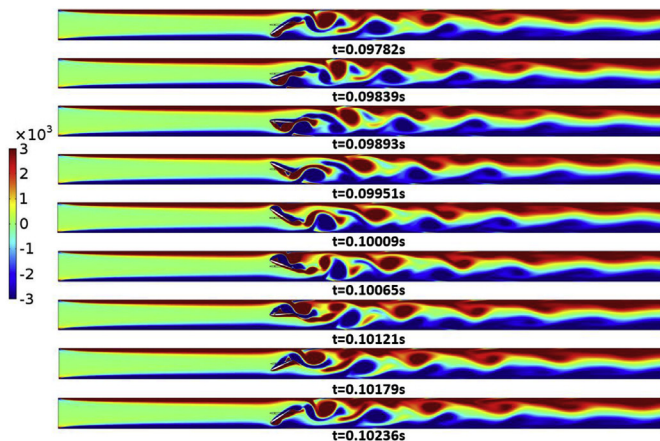


Fig. 19. Vorticity field in test case 2.

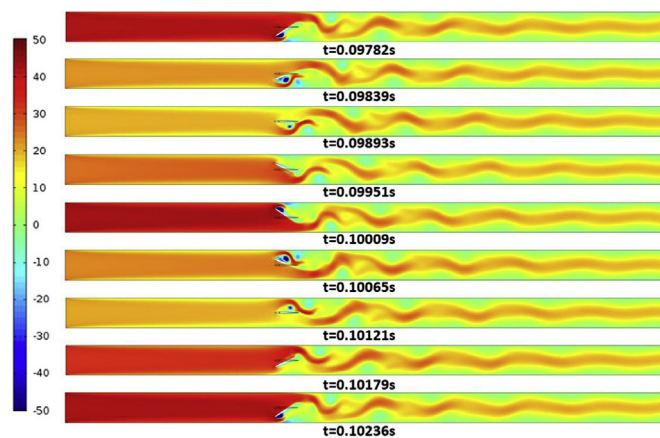


Fig. 20. Gauge pressure field in test case 2.

The self-agitator block ratio to the channel also reaches its extreme. Meanwhile, the pressure loss through the whole channel is at its highest. With the vortex growth and shedding process, the pressure loss

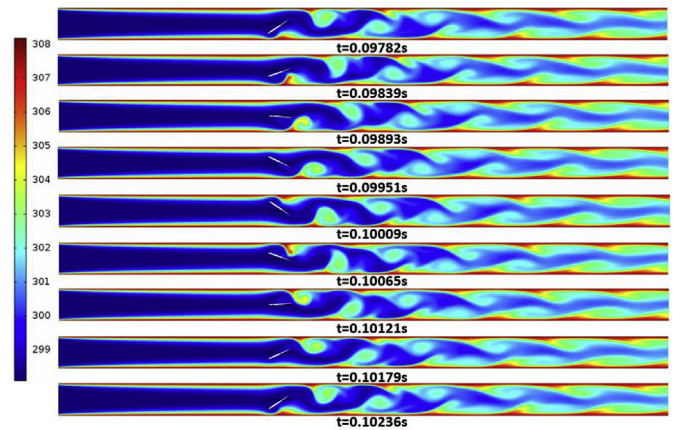


Fig. 21. Temperature field in test case 2.

decreases. Therefore, the main pressure loss increase is from the vortex generating process. When the leading edge is closest to the top boundary, the newly generated vortex causes the greatest pressure loss.

Fig. 15 shows the temperature fields for test case 1. Considering vortex generation and shedding processes, the temperature fields are directly related to the vorticity field. Temperature gradients near the boundaries increase at the vortices' location. Correspondingly, heat transfer in the channel is enhanced.

To investigate the effects on thermal performance, the local rejected heat and heat transfer coefficient are compared with clean channel results for  $t = 0.09696$  s. Fig. 16(a) shows the local heat transfer coefficient comparison which is defined as

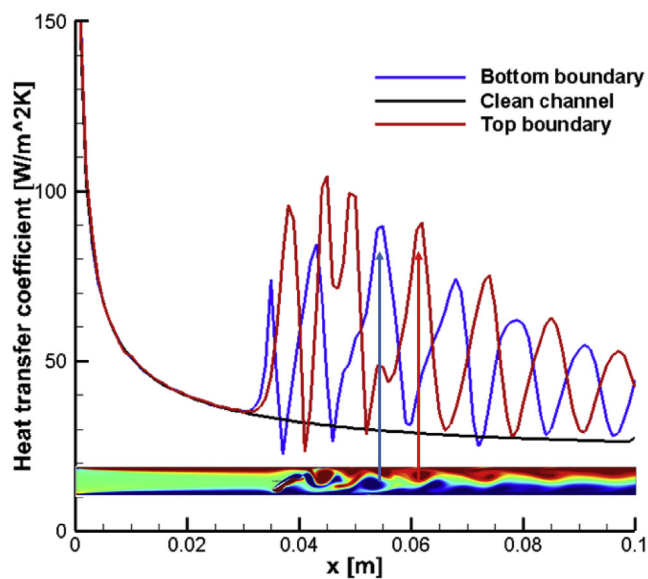
$$h = \frac{q}{T_{wall} - T_{average}}, \tag{10}$$

where  $q$  is the local heat flux and  $T_{average}$  is the average temperature for the local cross section. The heat transfer coefficients are highest at the inlet due to entrance effects. In comparison with the clean channel, the local heat transfer coefficients are not affected until near the location of self-agitator. Several peaks exist on both the top and bottom boundaries behind the self-agitator. These peaks have the same location as the highlighted vortices. Fig. 16(b) shows the local rejected heat comparison which has roughly the same profile as the heat transfer coefficient. The local average temperature in the channel with the self-agitator is higher than the clean channel because of the enhanced convection due to the vertical flow motion. Therefore, enhancement of the local heat transfer coefficient is higher than the enhancement of the local rejected heat.

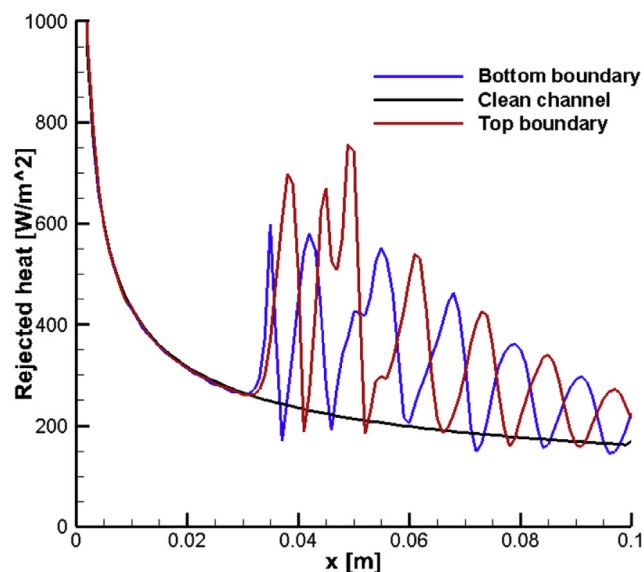
#### 4.2. Test case 2 results

In test case 2, the velocity is increased to 3.763 m/s while  $k_h k_h$ ,  $\beta_h$  and  $k_\theta$  are 96.6 N/m<sup>2</sup>,  $5.31 \times 10^8$  N/m<sup>4</sup> and  $5 \times 10^{-5}$  N, respectively. Then the self-agitator oscillates in the channel without touching the boundary. Fig. 17 shows the rotation center heave motion and rotation motion. The heave motion oscillates between  $-1.1$  mm and  $1.1$  mm, while the rotation motion oscillates between  $-0.6$  rad and  $0.6$  rad. Comparing the time to reach the extreme values, the heave and rotation motions are out-of-phase, which is the same as in case 1. Fig. 18 shows the Fourier analysis results for heave and rotation motions. These two motions' frequencies are both 220 Hz. The motions in test case 1 and 2 are also quite close with the main difference being that test case 2 has a higher frequency.

Figs. 19–21 show the vorticity field, gauge pressure field, and temperature field for test case 2. From the vorticity field results in



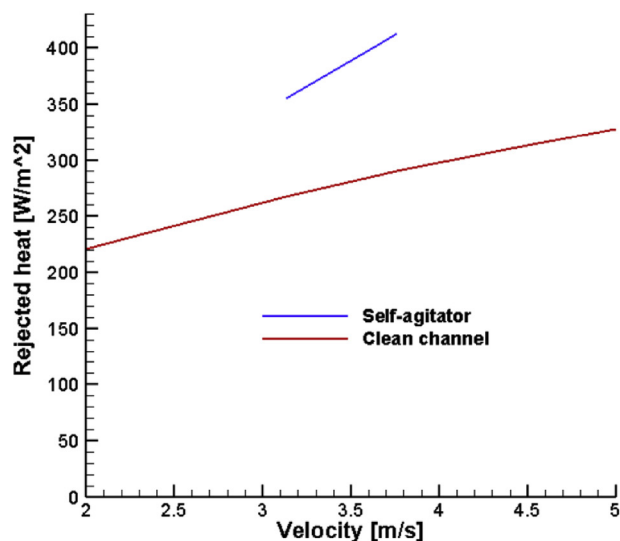
(a). Heat transfer coefficient comparison



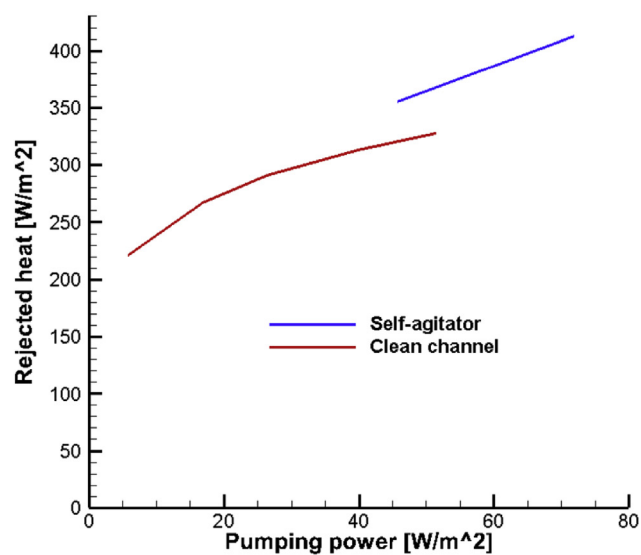
(b). Rejected heat comparison

Fig. 22. Local thermal performance comparison in test case 2.

Fig. 19, generation of a counterclockwise vortex and clockwise vortex begin when the distance between the leading edge and the bottom boundary reaches its lowest value. The vortices grow and start shedding when the self-agitator begins moving towards the top boundary. Then, this process starts again when the distance between the leading edge and the top boundary reaches its lowest value. This phenomenon agrees well with the results from test case 1. The vortices generated in test case 2 are stronger compared with those in test case 1. Fig. 20 shows the pressure field in test case 2 where the vortex generation process causes most of the pressure loss through the channel. The pressure loss is also higher than in test case 1 because of the formation of stronger vortices. Fig. 21 shows the temperature field for test case 2 where it is apparent that the mixing in the channel is also better, resulting in a higher temperature gradient at the top and bottom boundaries.



(a). Rejected heat changing with velocity



(b). Rejected heat changing with pumping power

Fig. 23. Thermal performance comparison between the channel with the self-agitator and the clean channel.

Fig. 22 shows the local thermal comparison between a channel with a self-agitator and a clean channel for  $t = 0.10236$  s. As shown in Fig. 22(a), the results for a channel with a self-agitator and those for a clean channel are in good agreement for the channel section to the left of the agitator. Several peaks exist in the channel with the self-agitator and correspond to the vortices' positions as highlighted. Vortices decay in the downstream direction, resulting in declining enhancement in the heat transfer coefficient. Fig. 22(b) shows the rejected heat comparison, which has the same tendency as that of the heat transfer coefficient. It is clear that, to enhance the heat transfer, we need to generate strong vortices.

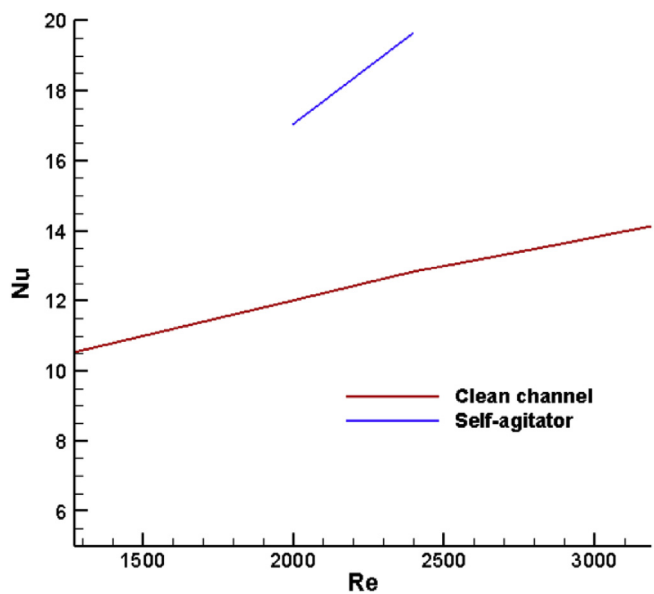


Fig. 24. Non-dimensional performance of self-agitator.

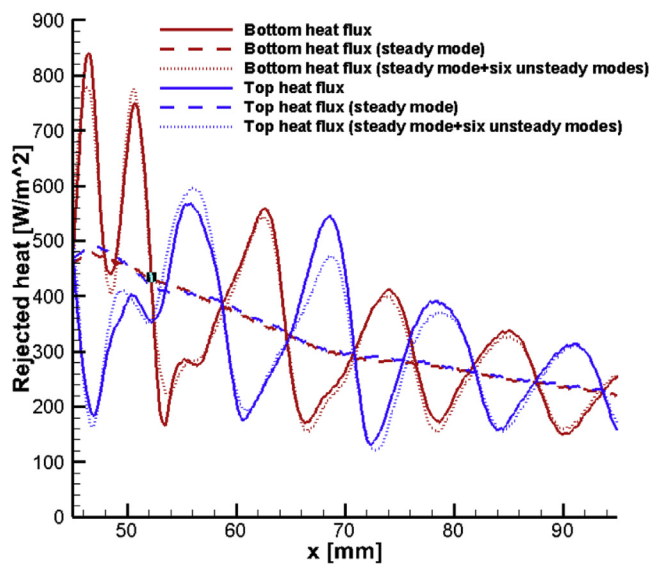


Fig. 27. Local performance from simulation and modal analysis.

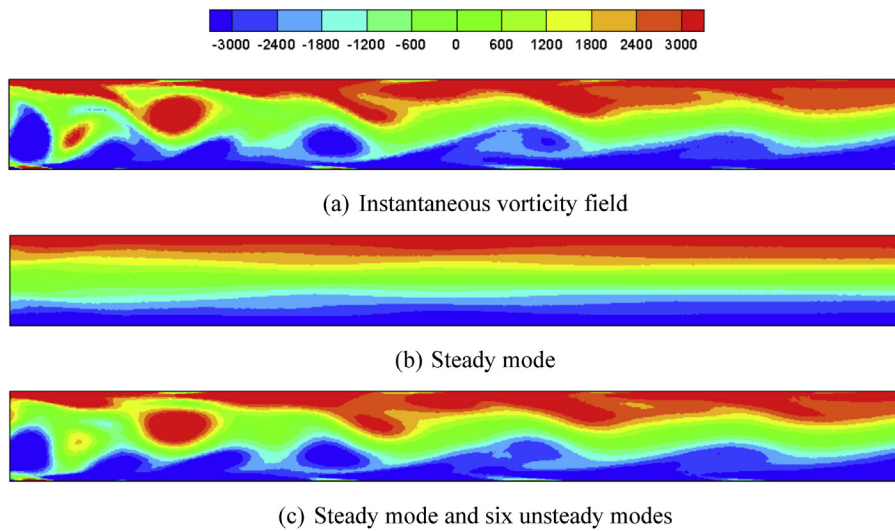


Fig. 25. Modal analysis for vorticity field.

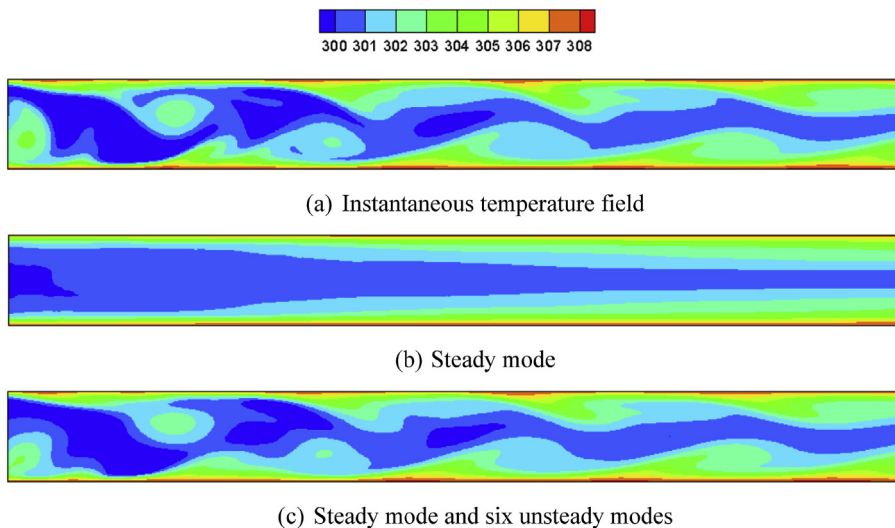


Fig. 26. Modal analysis for temperature field.

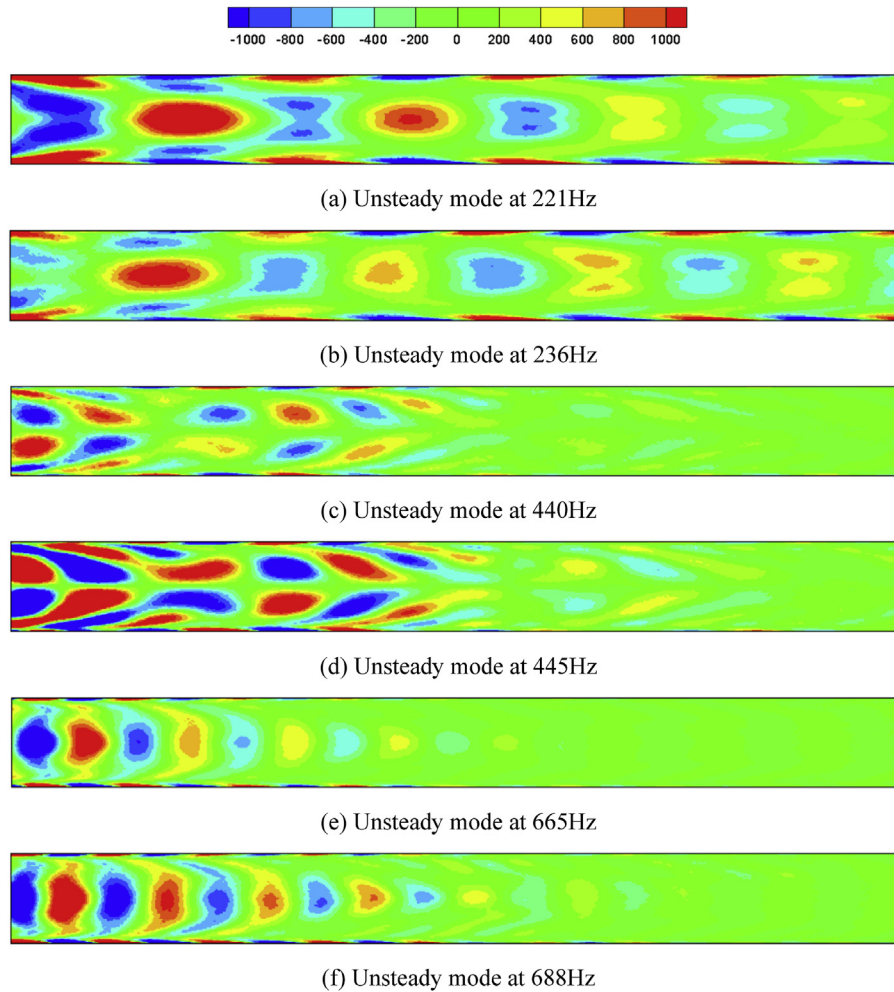


Fig. 28. Dominant unsteady modes in vorticity field.

#### 4.3. Thermal performance

Fig. 23 shows thermal performance comparison between the channel with the self-agitator and the clean channel control. As shown in Fig. 23(a), the self-agitator can enhance the heat transfer by 42% at the same velocity. The addition of a self-agitator also increases the pressure loss in the channel, so pumping power is employed to make a reasonable comparison, and is given as

$$\text{Pumping power} = \text{pressure loss} \times \text{velocity}. \quad (11)$$

As shown in Fig. 23(b), at the same pumping power the self-agitator can enhance heat transfer by 27%. Therefore, the self-agitator can enhance heat transfer in existing clean channel heat exchangers without additional power costs.

The self-agitator design is not limited to this specific channel. Non-dimensional performance of the self-agitator can be achieved based on the two test case results. The average Nusselt number is the non-dimensional parameter used to evaluate the convective heat transfer capability, which is defined as

$$Nu_{ave} = \frac{h_{ave} D_h}{k}, \quad (12)$$

where the average heat transfer coefficient,  $h_{ave}$ , is calculated as the rejected heat divided by the logarithmic mean temperature difference.

Fig. 24 shows the results of channels with self-agitators compared with the clean channel. With the same Reynolds number, the self-agitator can improve the Nusselt number by 52%.

#### 4.4. Modal analysis for temperature and vorticity fields

As previously discussed, a self-agitator can oscillate due to the fluid-structure interaction in the channel to increase mixing for heat transfer enhancement. However, the fundamental relation between the convective heat transfer enhancement and vorticity field is still lacking. To explore this, dynamic modal decomposition (DMD) [29]– [31] is performed with the transient numerical results in vorticity and temperature fields for test case 2. The computational region in DMD needs to be fixed, therefore, we choose the vorticity and temperature fields downstream of the self-agitator in the modal analysis. Steady and unsteady modes with fixed frequencies are achieved in the modal analysis for the temperature and vorticity fields. Fig. 25 shows the DMD results for the vorticity field; results reconstructed from the steady mode and first six dominant unsteady modes can provide a good prediction for the instantaneous simulation results. Fig. 26 shows the corresponding DMD results for the temperature field and instantaneous simulation results can also be reconstructed from the steady mode and first six dominant unsteady modes.

Fig. 27 shows the local performance obtained from the

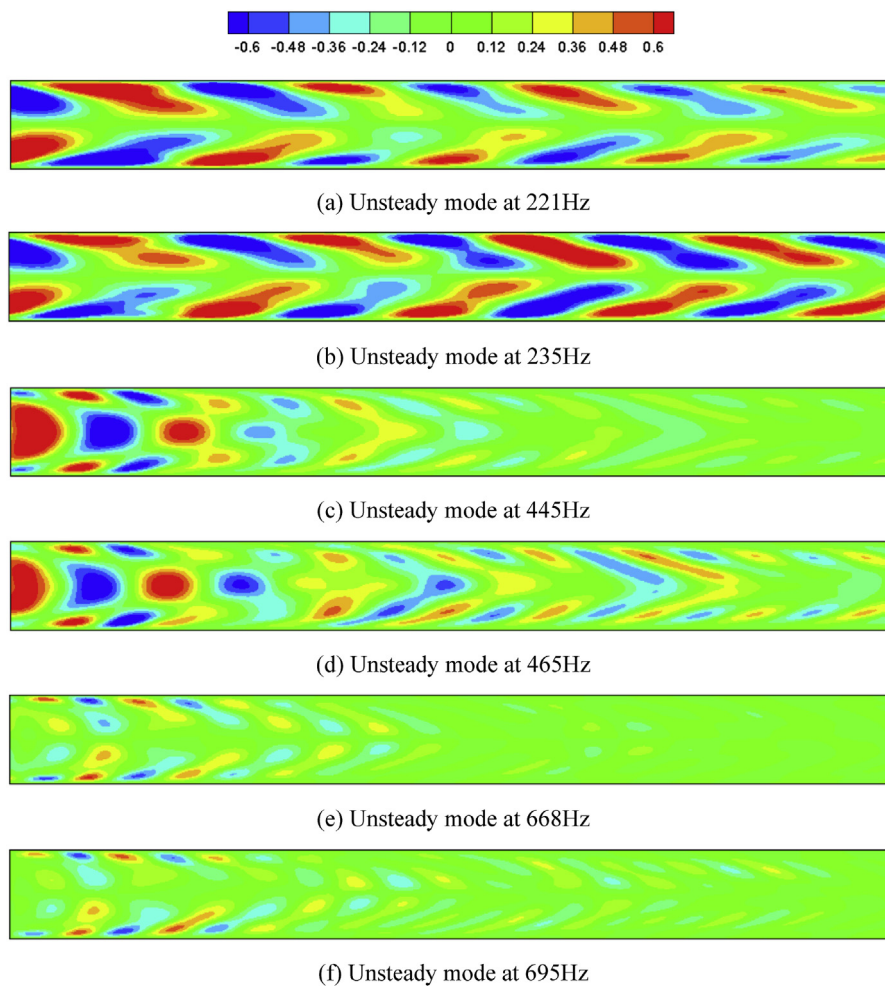


Fig. 29. Dominant unsteady modes in temperature field.

instantaneous simulation and modal analysis. As discussed in Figs. 16 and 22, rejected heat peaks appear at the vortices locations and their locations change as the vortices move in the channel. The reconstructed results from the steady mode and first six dominant unsteady modes agree well with those from the instantaneous simulation while the steady mode cannot reflect the peaks. The average rejected heats from the instantaneous simulation, steady mode and reconstruction results are  $326 \text{ W/m}^2$ ,  $325 \text{ W/m}^2$  and  $326 \text{ W/m}^2$ , respectively, and are in close agreement. Therefore, the average rejected can be predicted by the steady mode.

Figs. 28 and 29 show the first six unsteady modes and corresponding frequencies for vorticity and temperature fields. Each unsteady mode of temperature corresponds to one unsteady mode of vorticity and their frequencies are very close. As discussed in section 4.2, the self-agitator oscillates at 220 Hz from the Fourier analysis results while the frequencies of the first unsteady modes in vorticity and temperature fields are both  $\sim 220 \text{ Hz}$ . Therefore, the first unsteady mode is introduced by the self-agitator oscillation directly while the other dominant modes are introduced by the self-agitator oscillation and geometric channel effects.

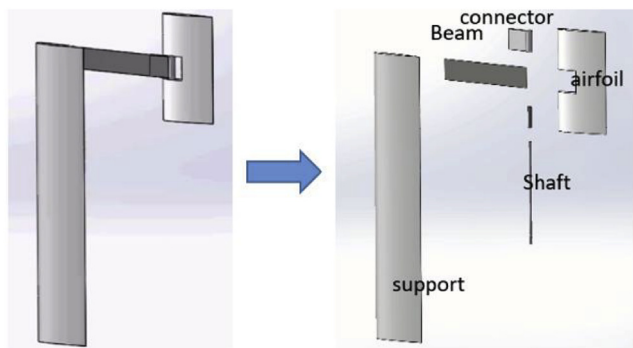
## 5. Experimental results

In section 4, a self-agitator was numerically shown to provide heat transfer enhancement. To further demonstrate the heat transfer

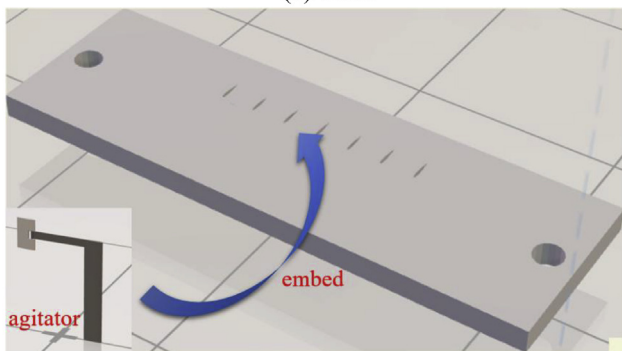
enhancement capability of the self-agitator, a prototype is fabricated for experimental testing in this section. Fig. 30(a) shows each self-agitator is composed with a support section, beam, connector, tube, shaft and airfoil. The support, connector and airfoil are made of 3D printed material while the rest parts are carbon steel with a thickness of 0.025 mm. The beam acts as a spring to control the airfoil movement. After that, the self-agitator is embedded in a support, which is part of the channel top as shown in Fig. 30(b). One self-agitator prototype is shown in Fig. 31 and it is tested in the experimental setup validated in section 3.2.

Besides the thermal performance test, the motion of one self-agitator in one period is captured with a high-speed camera with 3 m/s inlet velocity. Out-of-phase heave and rotations can be found in Fig. 32, which agree with the results presented in the previous numerical investigation. The oscillation frequency is 30 Hz, which is much lower than the one obtained numerically. This is because the spring constants in the numerical and experimental analyses are different. The lower frequency is preferred in the experimental test with regards to the fatigue life, which is discussed in the supporting material 1.

Fig. 33 shows the thermal performance of channel with a self-agitator compared with the clean channel case. The self-agitator can improve the rejected heat by 26% at same velocity as shown in Fig. 33(a). The pressure loss also increases after the self-agitator installation. Fig. 33(b) shows that the self-agitator can enhance the heat transfer by 15% at same pumping power. With nondimensional analysis, the self-



(a) Parts



(b) Installation

Fig. 30. Model for self-agitator.



Fig. 31. Self-agitator prototype.

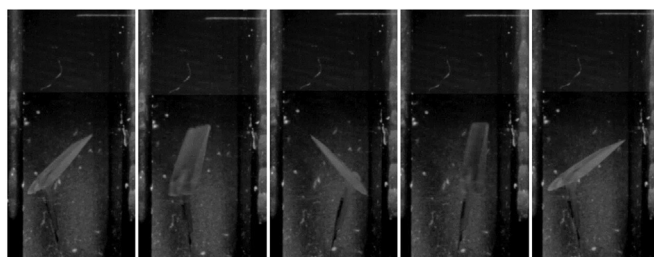


Fig. 32. Motions of self-agitator in one period captured with high speed camera.

agitator can improve Nusselt number by 34% at same Reynolds number.

The heat transfer enhancement ratio in our experimental test is lower than that in the 2-D numerical investigation. This could be caused by the lower oscillation frequency of the self-agitator. As discussed in the modal analysis in section 4.4, the average rejected heat is directly related to the steady mode and some unsteady mode has the same frequency as the one in structure vibration. However, the oscillation frequencies in experimental and numerical investigations are distinct. Therefore, the numerical and experimental unsteady modes are not same. As a result, the difference of thermal performance between the numerical and experimental results implies that adjusting the unsteady modes can influence the steady mode and affect performance.

**6. Conclusions**

A novel self-agitator is developed for heat transfer enhancement and it is demonstrated with numerical and experimental investigations. From the numerical results, the self-agitator can improve heat transfer by 42% at the same velocity and 27% at same pumping power, while the Nusselt number can be improved by 52% at the same Reynolds number, compared with a clean channel. Modal analysis is performed with numerical transient vorticity and temperature fields to explore the fundamental relation between the convective heat transfer enhancement and vorticity field. Instantaneous simulation results can be reconstructed with the steady mode and first six dominant unsteady modes, while the average rejected heat can be calculated from the steady mode directly. Moreover, the first dominant unsteady mode frequency is very close to that of the self-agitator oscillation. Therefore, the first unsteady mode is introduced by the self-agitator oscillation directly while the other dominant unsteady modes are introduced by the self-agitator oscillation and geometric channel effects.

A prototype of the self-agitator was fabricated and tested experimentally. Out-of-phase heave and rotation motions can be found from the motions captured with a high-speed camera, which agree with the results obtained in the numerical investigation. To achieve the desired fatigue life, the experimentally observed self-agitator frequency is lower than our numerical results. From the experimental results, the self-agitator can improve heat transfer by 26% at the same velocity and 15% at the same pumping power, while the Nusselt number can be improved by 34% at the same Reynolds number, compared to the clean channel case. The difference between the numerical and experimental results demonstrate that adjusting the unsteady modes could influence the steady mode to achieve different performance.

**Acknowledgements**

The authors greatly appreciate the support of ARPA-E under Grant No. DE-AR0000582. The authors would like to acknowledge Brian J.

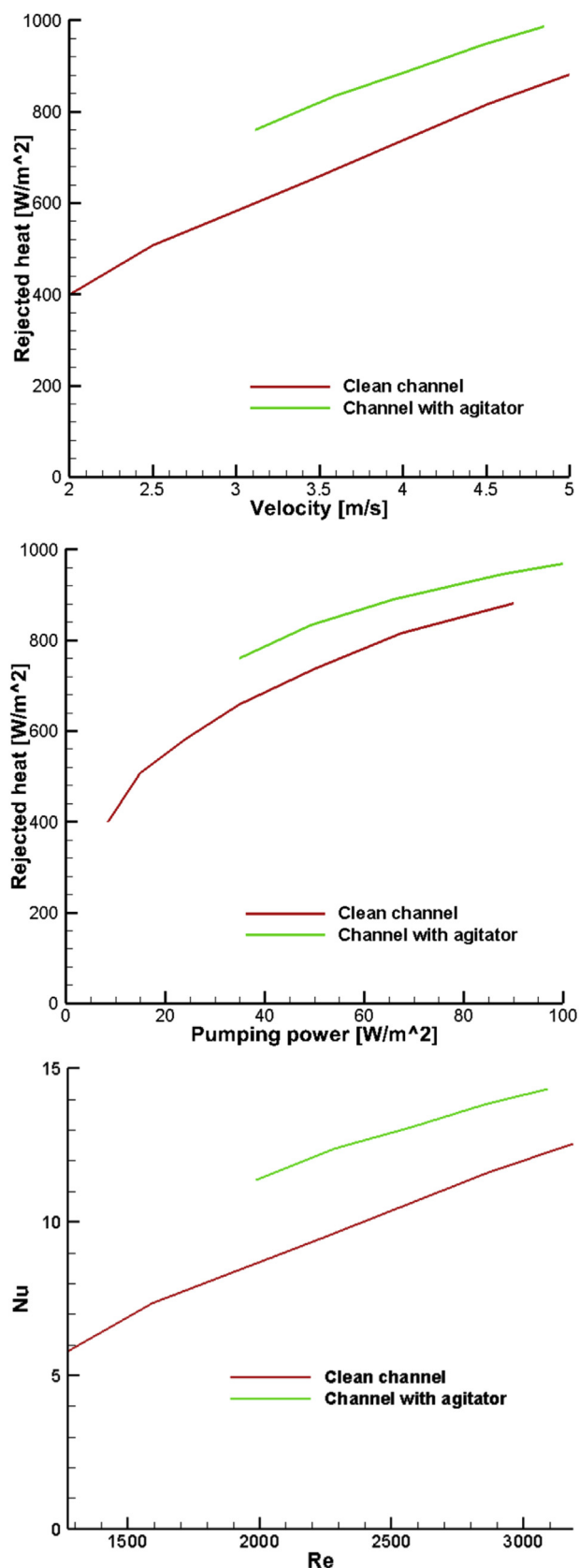


Fig. 33. Thermal performance for self-agitator.

Hernan and Miles V. Barnhart for their constructive comments.

#### Appendix A. Supplementary data

Supplementary data related to this article can be found at <https://doi.org/10.1016/j.ijthermalsci.2018.07.038>.

Supplementary video related to this article can be found at <https://doi.org/10.1016/j.ijthermalsci.2018.07.038>.

#### References

- [1] Z. Li, M. Yang, Y. Zhang, Hybrid lattice Boltzmann and finite volume method for natural convection, *J. Thermophys. Heat Tran.* 28 (1) (Jan. 2014) 68–77.
- [2] H. Xu, H.-H. Chen, S. Wang, Z. Li, K. Li, G. Stecker, W. Pan, J.-J. Lee, C.-L. Chen, Coupled natural convection and radiation heat transfer of hybrid solar energy conversion system, *Int. J. Heat Mass Tran.* 107 (2017) 468–483.
- [3] Z. Li, M. Yang, Y. Zhang, Lattice Boltzmann method simulation of 3-D natural convection with double MRT model, *Int. J. Heat Mass Tran.* 94 (2016) 222–238.
- [4] Z. Li, M. Yang, Y. Zhang, A coupled lattice Boltzmann and finite volume method for natural convection simulation, *Int. J. Heat Mass Tran.* 70 (2014) 864–874.
- [5] W.S. Fu, B.H. Tong, Numerical investigation of heat transfer characteristics of the heated blocks in the channel with a transversely oscillating cylinder, *Int. J. Heat Mass Tran.* 47 (2) (2004) 341–351.
- [6] A. Beskok, M. Raisee, B. Celik, B. Yagiz, M. Cheraghi, Heat transfer enhancement in a straight channel via a rotationally oscillating adiabatic cylinder, *Int. J. Therm. Sci.* 58 (2012) 61–69.
- [7] B. Celik, M. Raisee, A. Beskok, Heat transfer enhancement in a slot channel via a transversely oscillating adiabatic circular cylinder, *Int. J. Heat Mass Tran.* 53 (4) (2010) 626–634.
- [8] M. Pourgholam, E. Izadpanah, R. Motamedi, S.E. Habibi, Convective heat transfer enhancement in a parallel plate channel by means of rotating or oscillating blade in the angular direction, *Appl. Therm. Eng.* 78 (2015) 248–257.
- [9] A.D. Becker, H. Masoud, J.W. Newbolt, M. Shelley, L. Ristroph, Hydrodynamic schooling of flapping swimmers, *Nat. Commun.* 6 (May) (2015) 1–8.
- [10] J. Bae, J. Lee, S. Kim, J. Ha, B.-S. Lee, Y. Park, C. Choong, J.-B. Kim, Z.L. Wang, H.-Y. Kim, J.-J. Park, U.-I. Chung, Flutter-driven triboelectrification for harvesting wind energy, *Nat. Commun.* 5 (2014) 4929.
- [11] M.J. Shelley, J. Zhang, Flapping and bending bodies interacting with fluid flows, *Annu. Rev. Fluid Mech.* 43 (2011) 449–465.
- [12] N. Srinil, Multi-mode interactions in vortex-induced vibrations of flexible curved/straight structures with geometric nonlinearities, *J. Fluid Struct.* 26 (7–8) (2010) 1098–1122.
- [13] J.P. Gomes, H. Lienhart, Fluid–structure interaction-induced oscillation of flexible structures in laminar and turbulent flows, *J. Fluid Mech.* 715 (2013) 537–572.
- [14] M.L. Facchinetti, E. de Langre, F. Biolley, Coupling of structure and wake oscillators in vortex-induced vibrations, *J. Fluid Struct.* 19 (2) (2004) 123–140.
- [15] N. Srinil, H. Zanganeh, Modelling of coupled cross-flow/in-line vortex-induced vibrations using double Duffing and van der Pol oscillators, *Ocean Eng.* 53 (2012) 83–97.
- [16] A. Erturk, W.G.R. Vieira, C. De Marqui, D.J. Inman, On the energy harvesting potential of piezoaeroelastic systems, *Appl. Phys. Lett.* 96 (18) (2010).
- [17] V.C. Sousa, M. de M. Anicézio, C. De Marqui Jr., a Erturk, Enhanced aeroelastic energy harvesting by exploiting combined nonlinearities: theory and experiment, *Smart Mater. Struct.* 20 (9) (2011) 94007.
- [18] K. Kota, P. Hidalgo, Y. Joshi, A. Glezer, Hybrid liquid immersion and synthetic jet heat sink for cooling 3-D stacked electronics, *IEEE Trans. Compon. Packag. Manuf. Technol.* 2 (5) (2012) 817–824.
- [19] P. Hidalgo, A. Glezer, Direct actuation of small-scale motions for enhanced heat transfer in heated channels, *Annu. IEEE Semicond. Therm. Meas. Manag. Symp.* (2014) 17–23.
- [20] F. Herrault, P.A. Hidalgo, C.H. Ji, A. Glezer, M.G. Allen, Cooling performance of micromachined self-oscillating reed actuators in heat transfer channels with integrated diagnostics, *Proc. IEEE Int. Conf. Micro Electro Mech. Syst.*, no. February, 2012, pp. 1217–1220.
- [21] S. Ali, C. Habchi, S. Menanteau, T. Lemenand, J.L. Harion, Heat transfer and mixing enhancement by free elastic flaps oscillation, *Int. J. Heat Mass Tran.* 85 (2015) 250–264.
- [22] S.G. Park, B. Kim, C.B. Chang, J. Ryu, H.J. Sung, Enhancement of heat transfer by a self-oscillating inverted flag in a Poiseuille channel flow, *Int. J. Heat Mass Tran.* 96 (2016) 362–370.
- [23] Z. Li, X. Xu, K. Li, Y. Chen, G. Huang, C. Chen, C.-H. Chen, A flapping vortex generator for heat transfer enhancement in a rectangular airside fin, *Int. J. Heat Mass Tran.* 118 (2018) 1340–1356.
- [24] F. Casadei, K. Bertoldi, Wave propagation in beams with periodic arrays of airfoil-shaped resonating units, *J. Sound Vib.* 333 (24) (2014) 6532–6547.
- [25] F. Casadei, K. Bertoldi, Harnessing fluid-structure interactions to design self-regulating acoustic metamaterials, *J. Appl. Phys.* 115 (3) (2014).
- [26] K. Shoele, R. Mittal, Computational study of flow-induced vibration of a reed in a channel and effect on convective heat transfer, *Phys. Fluids* 26 (12) (2014).
- [27] X. Wang, S. Alben, The dynamics of vortex streets in channels, *Phys. Fluids* 27 (7) (2015).
- [28] K. Taira, S.L. Brunton, S.T.M. Dawson, C.W. Rowley, T. Colonius, B.J. McKeon,

- O.T. Schmidt, S. Gordeyev, V. Theofilis, L.S. Ukeiley, Modal Analysis of Fluid Flows: an Overview, (2017), pp. 1–46.
- [29] P.J. SCHMID, Dynamic mode decomposition of numerical and experimental data, *J. Fluid Mech.* 656 (2010) 5–28.
- [30] C.W. Rowley, S.T.M. Dawson, Model reduction for flow analysis and control, *Annu. Rev. Fluid Mech.* 49 (1) (2017) 387–417.
- [31] C.W. ROWLEY, I. MEZIĆ, S. BAGHERI, P. SCHLATTER, D.S. HENNINGSON, Spectral analysis of nonlinear flows, *J. Fluid Mech.* 641 (2009) 115.
- [32] K. Wang, A. Rallu, J.F. Gerbeau, C. Farhat, Algorithms for interface treatment and load computation in embedded boundary methods for fluid and fluid-structure interaction problems, *Int. J. Numer. Meth. Fluid.* 67 (9) (2011) 1175–1206.
- [33] X. Zeng, C. Farhat, A systematic approach for constructing higher-order immersed boundary and ghost fluid methods for fluid-structure interaction problems, *J. Comput. Phys.* 231 (7) (2012) 2892–2923.
- [34] S. Turek, J. Hron, Proposal for numerical benchmarking of fluid-structure interaction between an elastic object and laminar incompressible flow, *Lect. Notes Eng. Comput. Sci.* 53 (2006) 371.
- [35] F.-B. Tian, H. Dai, H. Luo, J.F. Doyle, B. Rousseau, Fluid–structure interaction involving large deformations: 3D simulations and applications to biological systems, *J. Comput. Phys.* 258 (2014) 451–469.
- [36] Z. Li, Y. Chen, X. Xu, K. Li, Z. Ke, K. Zhou, H. Chen, G. Huang, C. Chen, C. Chen, Air-side heat transfer enhancement with a novel self-agitator, *Proceedings of the ASME 2017 Heat Transfer Summer Conference*, 2017, pp. HT2017–4971.
- [37] Z. Li, Z. Ke, K. Li, X. Xu, Y. Chen, K. Zhou, H. Chen, G. Huang, C. Chen, Numerical and experimental investigations on longitudinal vortex generator for heat transfer enhancement in rectangular channel, *Proceedings of the ASME 2017 Heat Transfer Summer Conference*, 2017, pp. HT2017–4976.
- [38] Z. Li, Y. Chen, X. Xu, K. Li, Z. Ke, K. Zhou, G. Huang, H.-H. Chen, C.-L. Chen, C.-H. Chen, A novel air side heat transfer enhancement strategy with self-agitator, *47th AIAA Fluid Dynamics Conference*, 2017.
- [39] R.J. Moffat, Describing the uncertainties in experimental results, *Exp. Therm. Fluid Sci.* 1 (1) (1988) 3–17.